Biophysical Phenotyping and Modulation of ALDH+ Inflammatory Breast Cancer Stem-Like Cells

Weiqiang Chen,* Steven G. Allen, Weiyi Qian, Zifeng Peng, Shuo Han, Xiang Li, Yubing Sun, Chelsea Fournier, Liwei Bao, Raymond H. W. Lam, Sofia D. Merajver,* and Jianping Fu*

Cancer stem-like cells (CSCs) have been shown to initiate tumorigenesis and cancer metastasis in many cancer types. Although identification of CSCs through specific marker expression helps define the CSC compartment, it does not directly provide information on how or why this cancer cell subpopulation is more metastatic or tumorigenic. In this study, the functional and biophysical characteristics of aggressive and lethal inflammatory breast cancer (IBC) CSCs at the single-cell level are comprehensively profiled using multiple microengineered tools. Distinct functional (cell migration, growth, adhesion, invasion and self-renewal) and biophysical (cell deformability, adhesion strength and contractility) properties of ALDH+ SUM149 IBC CSCs are found as compared to their ALDH− non-CSC counterpart, providing biophysical insights into why CSCs has an enhanced propensity to metastasize. It is further shown that the cellular biophysical phenotype can predict and determine IBC cells' tumorigenic ability. SUM149 and SUM159 IBC cells selected and modulated through biophysical attributes—adhesion and stiffness—show characteristics of CSCs in vitro and enhance tumorigenicity in in vivo murine models of primary tumor growth. Overall, the multiparametric cellular biophysical phenotyping and modulation of IBC CSCs yields a new understanding of IBC's metastatic properties and how they might develop and be targeted for therapeutic interventions.

1. Introduction

Inflammatory breast cancer (IBC) is the most aggressive and lethal form of breast cancer with 20%–30% of patients presenting with metastasis at initial diagnosis.[1,2] Although RhoC GTPase and anaplastic lymphoma kinase are implicated in the IBC phenotype,[3,4] the underlying detailed mechanisms that allow IBC to be so aggressively metastatic from its inception are still under study. Recent evidence indicates that aldehyde dehydrogenase (ALDH) expressing subpopulation of IBC cells with stem cell-like properties (**Figure 1**a), termed "cancer stem-like cells" (CSCs),[5–7] plays a major role in the aggressive nature of IBC.[8] CSCs in various tumors have been shown to initiate tumorigenesis in numerous cancer types,[9–11] and recent studies have begun to define a role for CSCs in cancer metastasis as well.[8,12–14] Thus, specific targeting of these CSCs could be the key to effectively treating IBC. CSCs in different

Prof. W. Chen, W. Qian
Department of Mechanical and Aerospace Engineering
New York University
Brooklyn, NY 11201, USA
E-mail: wchen@nyu.edu

Prof. W. Chen
Department of Biomedical Engineering
New York University
Brooklyn, NY 11201, USA

Dr. S. G. Allen, Prof. S. D. Merajver
Program in Cellular and Molecular Biology
University of Michigan
Ann Arbor, MI 48109, USA
E-mail: smerajve@umich.edu

Z. Peng, S. Han, X. Li, Prof. J. Fu
Department of Mechanical Engineering
University of Michigan
Ann Arbor, MI 48109, USA
E-mail: jpfu@umich.edu

DOI: 10.1002/smll.201802891

Prof. Y. Sun
Mechanical and Industrial Engineering
University of Massachusetts
Amherst, MA 01003, USA

C. Fournier
Undergraduate Program in Neuroscience
University of Michigan
Ann Arbor, MI 48109, USA

L. Bao, Prof. S. D. Merajver
Department of Internal Medicine
University of Michigan Comprehensive Cancer Center
University of Michigan
Ann Arbor, MI 48109, USA

Prof. R. H. W. Lam
Department of Biomedical Engineering
City University of Hong Kong
Hong Kong, China

Prof. J. Fu
Department of Biomedical Engineering
Department of Cell and Developmental Biology
University of Michigan
Ann Arbor, MI 48109, USA
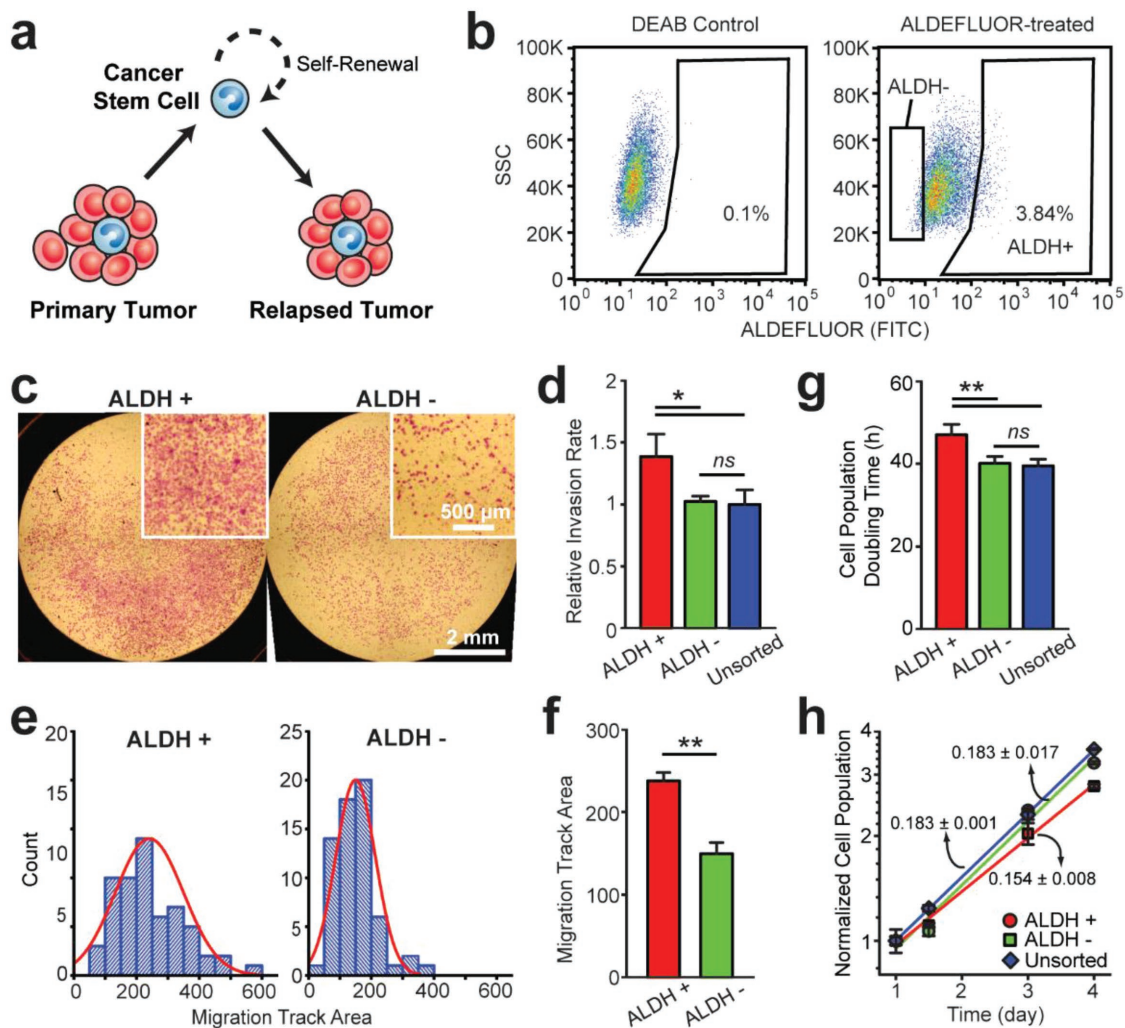
Figure 1. Functional phenotyping of IBC CSCs. a) Concept of cancer stem-like cells. b) Representative ALDEFLUOR analysis for SUM149 cells by FACS. Negative control samples (left) pretreated with DEAB inhibitor were used to ensure identification of ALDH+ and ALDH− cells (right). c) Representative images and d) quantitative data from in vitro invasion assays performed for ALDH+ and ALDH− SUM149 cells using the Biocoat Matrigel Invasion Chambers. In (c), invading cells were fixed with formaldehyde before being stained with 1% crystal violet. e) Distribution and f) average migration track area for single ALDH+ and ALDH− SUM149 cells measured by the Cellomics Cell Motility kit. g) Cell population doubling time and h) normalized cell population as a function of culture time determined using the MTT Cell Proliferation Assay Kit. For (d), (f), (g), and (h), error bars represent ± standard error of the mean (s.e.m.; $n = 4$). p-values were calculated using the student's t-test; ns ($p > 0.05$), * ($p < 0.05$), and ** ($p < 0.01$).

tumors have been characterized on the basis of their expression of particular surface markers[15,16]—such as CD133 and CD44—and also on the basis of cell adhesion molecules,[17] cytoprotective enzymes (e.g., ALDH),[18] and drug-efflux pumps (e.g., adenosine triphosphate-binding cassette transporters (ABC transporters)).[19] Identification of CSCs through specific marker expressions helps separate and define the CSC compartment; however, such molecular profiles may not fully capture the variety of changes in cell properties that foster ensemble effects in gross cellular behaviors, such as the highly aggressive and tumorigenic behaviors of IBC CSCs.

It is becoming increasingly clear that in vivo CSCs reside in a distinct microenvironment, the "CSC niche," in which a diverse array of environmental factors such as mechanical signals, adhesive, and soluble factor gradients contribute to the overall control of CSC phenotypes and activities. In response

to the CSC niche, cancer cells will adapt to many biophysical cues in their microenvironment and display distinct biophysical properties and plasticity to facilitate functional behaviors such as epithelial–mesenchymal transition (EMT), invasive, and metastatic activities. The integrative nature of cells that are embodied in the biophysical cellular mechanics may better capture the subtle and diverse changes in cell gene and molecular changes that cause the highly aggressive nature of IBC CSCs. However, how biophysical attributes of cancer cells are affected by biophysical cues and contribute to the emergence of IBC CSCs that underlie their ability to execute multiple metastatic events has not been previously undertaken.

Understanding the evolution of preferred biophysical phenotypes in IBC for CSC generation is desired for developing therapeutics that may potentially mitigate and further eradicate the CSC phenotypes in cancer. During metastatic progression,

**ADVANCED
SCIENCE NEWS**
www.advancedsciencenews.com

NANO · MICRO
small
www.small-journal.com

cancer cells encounter complex biophysical environments consisting of different degrees of extracellular matrix (ECM) cross-linking,[20] a differing ECM topology,[21–23] mechanical heterogeneity within the ECM,[24,25] as well as being exposed to shear flow and interstitial pressure.[26–28] In response, metastatic cancer cells must acquire unique biophysical characteristics in order to navigate through this dynamic microenvironment to reach and proliferate in distant sites. As CSCs are believed to play critical roles in metastasis, it is highly possible that CSCs too will develop biophysical properties—such as increased deformability and decreased adhesion strength—necessary to traverse this environment and be capable, for example, of repopulating tumor masses following treatment. Biophysical properties such as cell deformability, adhesion strength, and contractility are significantly important in cancer metastasis. In the first step of the metastatic cascade, decreased adhesion of cancer cells might indicate why those cells are able to migrate away from the primary tumor and those strongly adherent cancer cells might not be able to overcome their attachment. In the next steps of the metastatic cascade, migrating cancer cells must invade through the basement membrane and squeeze through endothelial cell tight junctions during intravasation and extravasation. A greater capacity for deformation enables successfully transition through a confining biophysical microenvironment. Cell deformability (i.e., compliance under an applied load) has been postulated to play key roles in cancer cell invasiveness.[29–32] Many studies have demonstrated a significantly higher degree of cell deformability for both cancer cell lines and primary tumors when compared to normal epithelial cells.[29–31,33] In the case of breast and ovarian cancers, the subpopulation of cancer cells with increased cell deformability has been shown to have a more malignant phenotype compared to stiffer cells.[29,34] These changes in adhesion and deformability further suggest significant plasticity toward cytoskeletal changes or reorganization and underlying biophysical differences in IBC CSCs. Cytoskeletal changes have been suggested to underlie biophysical differences observed in invasive cancer cells, consistent with a process of selection for cells that are able to squeeze into vessels by traversing walls (intravasate).[26,35,36] These cytoskeletal changes can be measured and demonstrated through measuring the traction forces generated by these cells and further suggest inherent differences in cell force generation correlated with aggressiveness. Cell contractility has previously been shown to mediate cell functions (e.g., migration, adhesion, and proliferation) as well as mechanotransduction.[37–42] Therefore, cell traction forces may also be involved in cancer progression. Previous studies have convincingly established the usefulness of biophysical characteristics for identifying more aggressive cancer cells in a label-free manner that is independent of current immunohistological methods.[29,33,35,43,44]

Given that IBC is the most aggressive and metastatic breast cancer, a comprehensive, multiparametric phenotypic profiling of CSCs can provide useful insights into the qualities of IBC CSCs that increase their aggressiveness and propensity for tumorigenesis and metastasis, as well as allow for studies of novel therapeutic interventions targeting CSC functions. Here, we first comprehensively analyzed the intrinsic functional capabilities of ALDH+ SUM149 IBC's CSC compartment as well as these cells' inherent biophysical properties that make them capable of early metastasis, essentially from the tumor's inception. We prove that the biophysical features encoded in single cancer cells, or so-called "biophysical phenotype," can predict and determine the "stemness" and tumorigenic ability with more accuracy. Furthermore, we prove to utilize and modulate SUM 149 and SUM 159 IBC cells' biophysical properties to select aggressive CSCs and tune IBC cell toward a more "CSC-like" subtype with enhanced tumorigenic ability.

2. Functional Phenotyping of IBC CSCs

In this study, we first isolated breast CSCs with high ALDH enzymatic activity from an IBC cell line, SUM149, using an ALDEFLOUR assay (see the Experimental Section).[3] ALDH is a superfamily of detoxifying enzymes responsible for metabolizing a wide variety of intracellular aldehydes and plays an important role in multiple biological activities, including drug resistance, cell differentiation, and oxidative metabolism.[45–47] ALDH expression has been used as a predictive marker of CSCs for breast cancer[3,16,48,49]—including IBC[8]—and ALDH expression has proven to be more predictive than other established markers such as CD44+/CD24− for identification of breast CSCs, as it has been shown that ALDH can identify cells with a greater resistance to chemotherapy.[50,51] High activity of ALDH within tumors has been associated with a poor prognosis in many cancers including breast,[3,8,16,48] lung,[52,53] liver,[54] colon,[18,55] pancreatic,[56] ovarian,[57] head and neck,[58] and prostate[59] cancer. SUM149 cells were stained for ALDH using the ALDEFLOUR reagent and sorted by flow cytometry. ALDEFLUOR-treated cells quenched with the ALDH inhibitor diethylaminobenzaldehyde (DEAB) were used to set the ALDEFLUOR-positive fluorescence-activated cell sorting (FACS) gate, containing less than 0.1% of DEAB-treated cells (Figure 1b). SUM149 cells above this 0.1% fluorescence threshold were sorted as ALDH positive (ALDH+). ALDH negative (ALDH−) cells were sorted as the bottom percentage of cells that corresponded to the ALDH+ percentage (i.e., if 3.5% of cells were ALDH+, then the bottom 3.5% of cells were gated for the ALDH− population).

We performed comprehensive profiling to study functional phenotypes of ALDH+ IBC CSCs. First, the ratio of ALDH+ CSCs in the SUM149 cell line was quantified across multiple sortings to establish reliability (>20). The proportion of ALDH+ cells in the SUM149 cell line was between 1% and 7%, with an average of 3.93% ± 1.84%, similar to what has been reported previously.[8] Interestingly, the ALDH+ CSC population maintained a dynamic equilibrium in the SUM149 cell line. In a purified ALDH+ population, the percentage of ALDH+ cells gradually decreased from 100% to the normal level (3%–5%) for SUM149 cells over 3–5 d (data not shown), presumably by cell differentiation. Thus, the ALDH+ compartment was able to recapitulate the heterogeneity of the parent cell population by maintaining an almost constant percentage of ALDH+ CSCs, consistent with previously reported results.[8,60,61]

To study the tumorigenic and metastatic potential of ALDH+ SUM 149 IBC CSCs, in vitro invasion, migration, and proliferation assays were conducted. In vitro invasion assays were performed using the Biocoat Matrigel Invasion Chamber (see the Experimental Section) to examine the ability of cancer cells to invade through a Matrigel membrane under a serum gradient, mimicking the basement membrane invasion process in cancer

ADVANCED
SCIENCE NEWS
www.advancedsciencenews.com

NANO · MICRO
small
www.small-journal.com

metastasis. As shown in Figure 1c,d, ALDH+ IBC CSCs were more invasive compared to the ALDH− population and the unsorted SUM149 control. We further examined cell motility by using the Cellomics Cell Motility kit to measure the migration area of ALDH+ and ALDH− cells. Each sorted cell type (ALDH+ and ALDH−) was plated in equal densities in three to five wells of a 96-well plate that had previously been coated with blue fluorescent microbeads. After 24 h of incubation, the area a cell migrated is represented by the negative space in the microbead carpet that has been pushed away or phagocytosed by the cell. This cell motility assay demonstrated a significantly higher motility for ALDH+ than ALDH− cells (Figure 1e,f), suggesting a more aggressive and motile phenotype for ALDH+ IBC CSCs. To evaluate the growth rates of ALDH+ and ALDH− cells, these populations were quantified and compared with unsorted SUM149 controls using 3-(4,5-dimethylthiazol-2-yl)-2,5-diphenyltetrazolium bromide (MTT) assays (see the Experimental Section). Cell populations of flow-sorted ALDH+ and ALDH− cells and unsorted SUM149 controls were measured at 24, 36, 72, and 96 h post sorting. As shown in Figure 1g,h, ALDH+ cells had a slower growth rate and significantly longer cell doubling time compared to ALDH− cells and unsorted control cells. This slower growth rate for ALDH+ cells suggests that the IBC CSCs can maintain a semi-quiescent or slowly cycling state, similar to the behavior of many adult stem cell types.

3. Biophysical Phenotyping of IBC CSCs

3.1. Cell Deformability Measurements for IBC CSCs

Our invasion assays demonstrated that ALDH+ cells had a greater capability to migrate through confined physical spaces, a process that necessitates significant cell shape and cytoskeleton (CSK) changes. Thus, we hypothesized that there would be a concomitant difference in cell deformability between ALDH+ and ALDH− cells. Furthermore, at a key step in the metastatic cascade, cell deformability has been postulated to play a key role in invasion through the basement membrane.[35,36] To explore potential differences in cell deformability between the ALDH+ SUM149 IBC CSCs and ALDH− subpopulations, we utilized a microfluidic-based deformability microcytometer especially designed for highly sensitive, high-throughput, and label-free quantification of cell deformability at the single-cell level.

The microfluidic deformability microcytometer was made of polydimethylsiloxane (PDMS) and contained an array of identical funnel-shaped, long confining microchannels that served to automatically direct and trap individual live cancer cells within each channel (**Figure 2**a and Figure S1 (Supporting Information)). The microchannel walls were precoated with Pluronic-127, a hydrophilic nonionic surfactant, so that friction between the cell and the channel wall would be negligible. Within the deformability microcytometer, differential hydrodynamic pressure acting on individual cancer cells gradually pushes the cell down the funnel and, ultimately, the motion of the cell stops and the cell is trapped due to confining space of the funnel-shaped channel. For inert microfluidic channels where cell trapping is dictated by steric interactions between cancer cells and the channel wall, the penetration length (L) of an individual cancer cell into the channel is completely determined by its cell volume and cell deformability (Figure 2a,b). Thus, the cell deformability of each cancer cell can be calculated (see the Experimental Section) based upon known or measured parameters including pressure, cell volume, and the penetration length L (or the distance d between the position
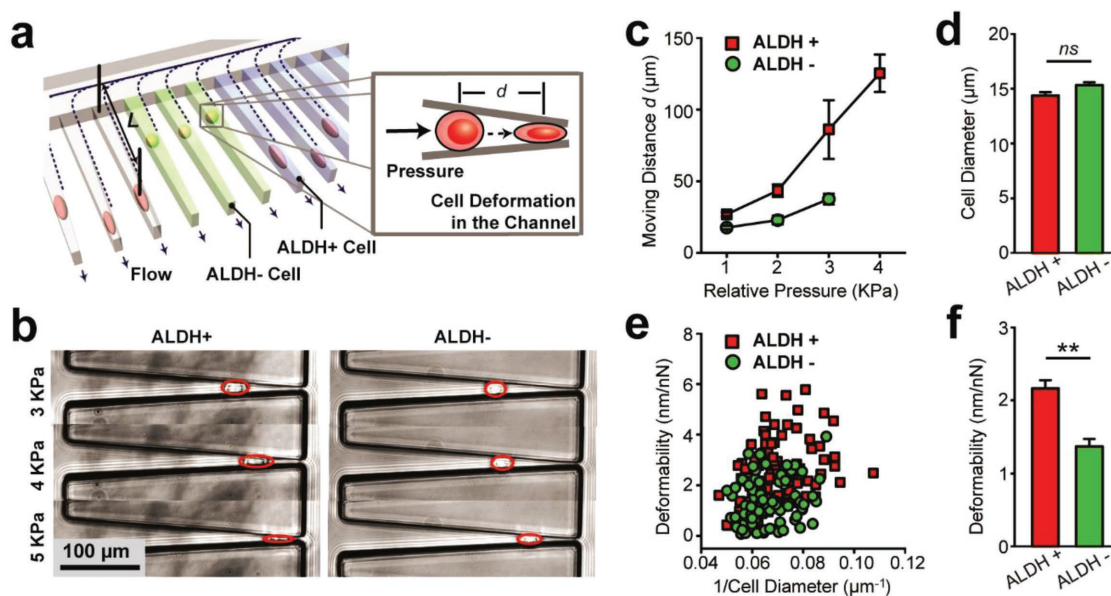
Figure 2. Cell deformability measurements for IBC CSCs. a) Schematic of microfluidic deformability microcytometer for single cell deformability measurements. b) Representative images and c) quantitative data showing differential penetrating distances for ALDH+ and ALDH− SUM149 cells in the deformability microcytometer under different pressures as indicated. d) Average cell diameter of ALDH+ and ALDH− SUM149 cells. e) Cell deformability plotted as a function of cell diameter. Each data point represents an individual cell. f) Average cell deformability of ALDH+ and ALDH− SUM149 cells. For (c), (d), and (f), error bars represent ± s.e.m. ($n > 100$). p-values were calculated using the student t-test; ns ($p > 0.05$) and ** ($p < 0.01$).

ADVANCED
SCIENCE NEWS
www.advancedsciencenews.com

NANO · MICRO
small
www.small-journal.com

where the cell started to deform and the final trapped position in the channel).

We quantified the cell deformability of both ALDH+ and ALDH− SUM149 cells using the deformability microcytometer, with results showing that under the same differential hydrodynamic pressure across the confining microchannels, the average penetration length *L* of ALDH+ IBC CSCs was significantly greater than that of ALDH− cells, while the cell diameters of both populations were comparable (Figure 2c,d). This suggested a greater deformability of ALDH+ SUM149 IBC CSCs than ALDH− cells. We further performed correlative studies using single cell data for cell deformability and cell diameter. Our analysis in Figure 2e showed no strong correlation between cell deformability and cell diameter for either ALDH+ or ALDH− cells, suggesting that cell deformability is an intrinsic biophysical property regardless of cell size. Interestingly, deformability of ALDH+ cells was distributed across a relatively higher range than ALDH− cells (Figure 2e,f), pointing to a potential inherent propensity and ability of ALDH+ SUM149 IBC CSCs to more readily undergo the necessary cytoskeletal rearrangement to intravasate across the basement membrane during invasion.

In addition to measurements for CSCs, we also compared the cell deformability of another noninflammatory and less aggressive breast cancer cell line (MCF-7) with the normal-like breast epithelial cell line (MCF-10A). Our results showed that MCF-7 cells exhibited greater cell deformability than MCF-10A cells (Figure S1c,d, Supporting Information). Together, our data show that the small population of ALDH+ SUM149 IBC CSCs possesses a higher cell deformability than normal breast cancer cells.

3.2. Cell Adhesion Strength Characterization for IBC CSCs

We conducted adhesion assays for SUM149 breast cancer cells to evaluate their ability to make stable physical contact with surfaces (**Figure 3**a,b) by using standard cell adhesion assay methods.[62,63] Three groups of SUM149 cancer cells, including sorted ALDH+ cells, ALDH− cells, and an unsorted control, were seeded at the same density as single cells in polystyrene 48-well cell culture plates. Three hours after cell seeding, floating cells were removed, and adherent cancer cells were stained with Calcein AM for visualization. Fluorescence images of stained cancer cells in the entire sample area were taken for quantification of the adhesion rate, defined as the ratio of the number of cells adhered to the surface to the total number of cells initially seeded per sample. Quantitative analysis revealed that ALDH+ SUM149 cells had a much lower adhesion rate compared to both the ALDH− population and unsorted control (Figure 3b). On average, the adhesion rate after 3 h of cell seeding was 25.6% for ALDH+ cells, while for ALDH− cells and unsorted control cells the adhesion rates were 60.6% and 52.0%, respectively.

Our results in Figure 3a,b demonstrating a significant difference in the adhesion properties of ALDH+ and ALDH− SUM149 cancer cells suggested the possibility that adhesion strength of cancer cells might similarly be correlated with ALDH expression as was cell deformability. To examine specifically the possibility of the IBC CSC compartment consisting of intrinsically less adherent cells, we developed a microfluidic cell adhesion assay for direct measurements of the adhesion strength of cancer cells (Figure 3c; see the Experimental Section). Shear stress-based measuring of cell adhesion strength in microfluidic devices has been previously reported.[64] The adhesion strength of cancer cells is defined as the fluidic shear stress at which 50% of cancer cells initially adherent on the microfluidic channel detach after being exposed to shear stress.[65–67] A low density of ALDH+ or ALDH− SUM149 IBC cells was seeded uniformly on the glass substrate in a microfluidic channel for 12 h before they were exposed to constant directional fluid shear (0.1–320 dyne cm^{-2}) for 3 min. We quantified the fraction of cancer cells remaining adherent in the microfluidic channel after exposure to this sustained 3 min directional fluid shear. Our data demonstrated that indeed the ALDH+ SUM149 IBC CSCs were only capable of withstanding much lower fluidic shear stresses than the ALDH− cells (Figure 3d,e). Adhesion strength was significantly lower for ALDH+ SUM149 IBC CSCs than ALDH− cells (Figure 3f). Together, our results in Figure 3 demonstrated that adhesive properties could be quantitatively delineated and correlated with the ALDH-defined IBC CSC population in the SUM149 cell line. ALDH+ SUM149 IBC cells had a decreased ability to adhere to a substrate and overall decreased adhesion strength.

3.3. Cell Traction Force Measurements for IBC CSCs

The difference seen in cell adhesion properties between ALDH+ SUM149 IBC CSCs and ALDH− cells implicated an involvement of actin cytoskeleton and integrin-mediated focal adhesions that tether the actin CSK to the ECM. To investigate this hypothesis, we utilized a PDMS micropost array (PMA) as subcellular live-cell force sensors to quantify intracellular CSK contractile forces (**Figure 4** and Figure S2, Supporting Information).[68–70] This PMA consists of hexagonally spaced, vertical, elastomeric posts fabricated using replica molding with PDMS from microfabricated silicon masters (Figure 4a and Figure S2a–d, Supporting Information). After adhesive proteins are coated on the post tips using microcontact printing (Figure S2, Supporting Information; see the Experimental Section), cells are able to adhere, spread out, and exert contractile forces that deflect the underlying posts (Figure 4a–d and Figure S2c, Supporting Information). Each post, therefore, functions as a cantilever and force sensor, capable of measuring local cellular traction force exerted at the post tip (Figure S2e–g, Supporting Information).[68–70]

We performed quantitative analysis of cell morphology and CSK contractility of SUM149 cells with the PMA (Figure 4e,f). Our results revealed that the total cell traction force was significantly less for ALDH+ cells compared to ALDH− ones (Figure 4g). Previous studies have demonstrated that cell traction force generation can be confounded by a cell's footprint area.[39,40,68] To exclude the possibility that the decreased cell traction force for ALDH+ CSCs was simply caused by a variance in cellular area, we quantified cell spread area for SUM149 cells. Our results in Figure 4h showed no significant difference in cell spread area between ALDH+ and ALDH− cells. To further investigate the role of cell spread area in the generation

ADVANCED
SCIENCE NEWS
www.advancedsciencenews.com

NANO · MICRO
small
www.small-journal.com
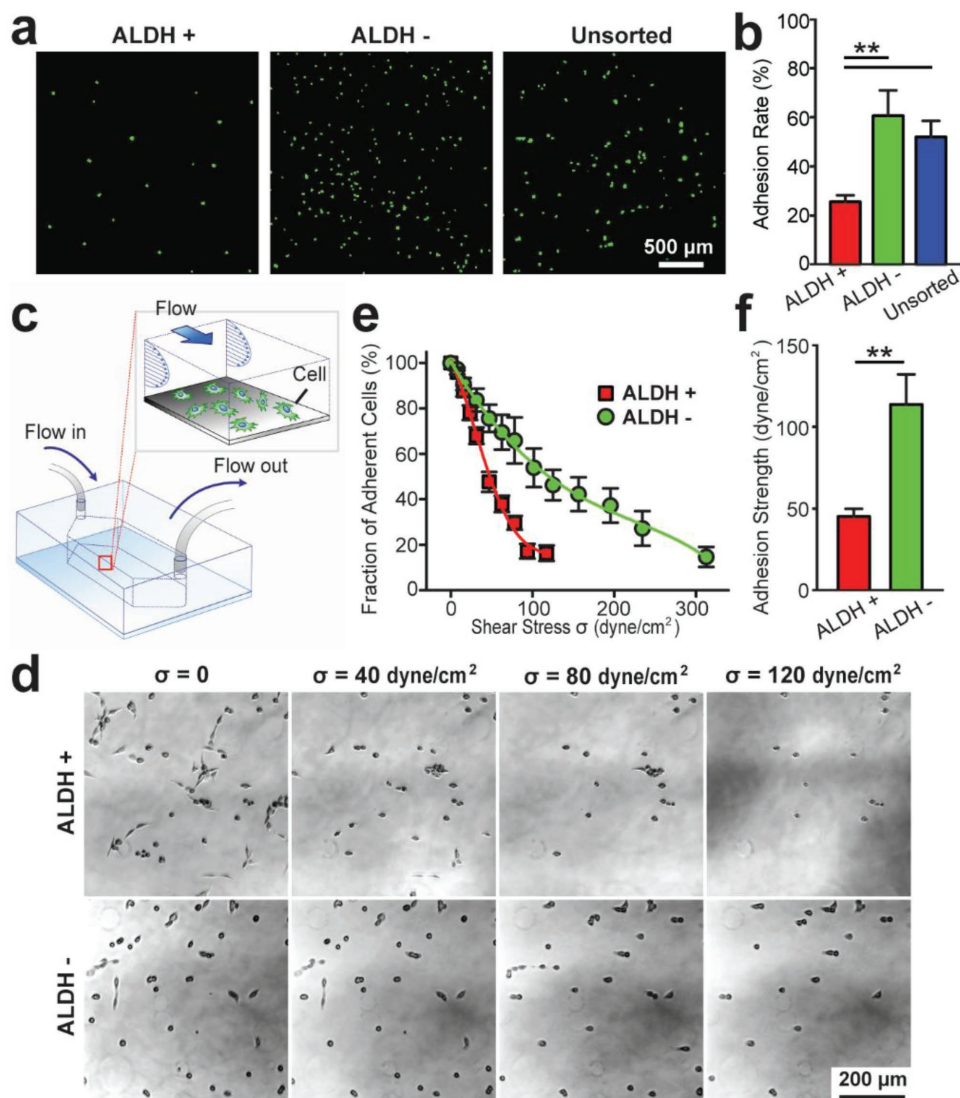
Figure 3. Cell adhesion strength characterization. a) Representative fluorescence images and b) quantified adhesion rate of ALDH+, ALDH−, and unsorted SUM149 cells adhering to polystyrene 48-well cell culture plates 3 h after cell seeding. Cells were stained with Calcein AM for visualization and enumeration. c) Schematic of a microfluidic channel for quantification of cell adhesion strength. The inset shows adherent cancer cells in the channel under sustained directional fluid shear. d) Representative brightfield images showing temporal sequences of ALDH+ and ALDH− SUM149 cells detaching from the microfluidic channel under increased fluid shear stress. e) Fraction of ALDH+ and ALDH− SUM149 cells remaining adherent in the microfluidic channel after 3 min exposures to sustained directional fluid shear. Low densities of cancer cells were seeded into microfluidic channels and cultured for 12 h before PBS was flowed continuously along the channel to exert fluid shear stress on cells. Solid lines represent logistic curve fitting. f) Adhesion strength of ALDH+ and ALDH− SUM149 cells. For (b), (e), and (f), error bars represent ± s.e.m. ($n = 4$). p-values were calculated using the student t-test; ns ($p > 0.05$) and ** ($p < 0.01$).

of traction forces, we analyzed the total traction force of each cell normalized by its spread area (traction force per cell area), with results showing that the average traction force per cell area was lower for ALDH+ SUM149 IBC CSCs compared to ALDH− SUM149 cells (Figure 4i). Hence, these results indicate that the smaller traction forces exerted by ALDH+ IBC CSCs versus ALDH− cells are not linked to differences in cell spread area, but to other inherent cellular differences between the two populations. Consistent with previous reports though,[39,40,68] within the same group of cells (ALDH+ or ALDH−) the correlative plot (Figure 4j) of single-cell data of total traction force

and cell spread area did show a strong linear correlation of increasing traction force with cell spread area. However, the slope of the linear correlation between the traction force and cell spread area was substantially less for ALDH+ cells than for ALDH− cells (0.13 nN μm^{-2} vs 0.07 nN μm^{-2}), again indicating distinct biophysical properties of ALDH+ and ALDH− cells. Our traction force study in conjunction with the adhesion strength results indicates that ALDH+ and ALDH− cells have differential biophysical properties with the ALDH+ SUM149 IBC CSCs being less adherent and exerting less contractile force. This may help explain the metastatic potential difference

ADVANCED
SCIENCE NEWS
www.advancedsciencenews.com

NANO · MICRO
small
www.small-journal.com
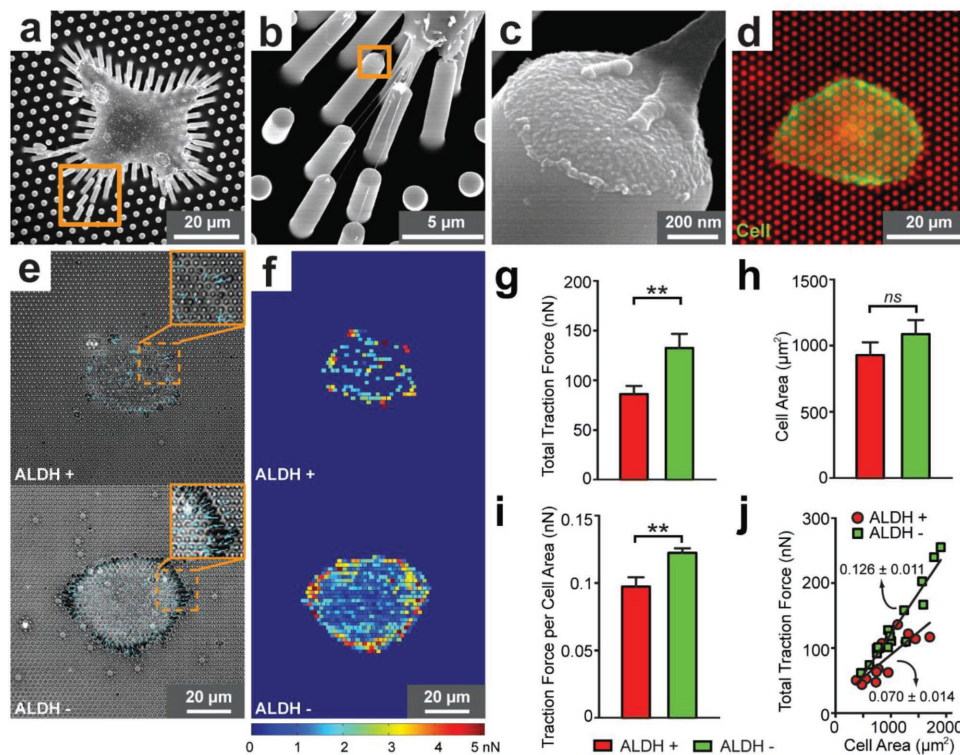
Figure 4. Quantification of cell traction force. a–c) Representative SEM and d) immunofluorescence images showing single SUM149 cells adherent on the PDMS micropost array. In (d), the single SUM149 cell was stained with fluorophore-labeled phalloidin for visualization of actin filaments (green). The underlying PDMS posts were labeled with DiI for visualization. e) Phase and f) colorimetric maps showing subcellular traction forces exerted by single ALDH+ (top) and ALDH– (bottom) SUM 149 cells on the PDMS microposts. g–j) Quantitative analysis of cell morphology and traction force. g) Plot total traction force per cell, h) total cell spread area, and i) traction force per cell area for single ALDH+ and ALDH– cells. Data represent the means ± s.e.m. ($n > 15$). p-values were calculated using the student t-test; ns ($p > 0.05$) and ** ($p < 0.01$). j) Total traction force per cell as a function of cell spread area. Each data point represents an individual cell. Data trends in (j) are plotted using linear least square fitting (black lines), with slope values ± s.e.m. indicated.

between the ALDH+ and ALDH– populations. Cells that are prone to forming strong connections with their surrounding ECM (ALDH– cells) may be less likely to successfully migrate away from the primary tumor.[71]
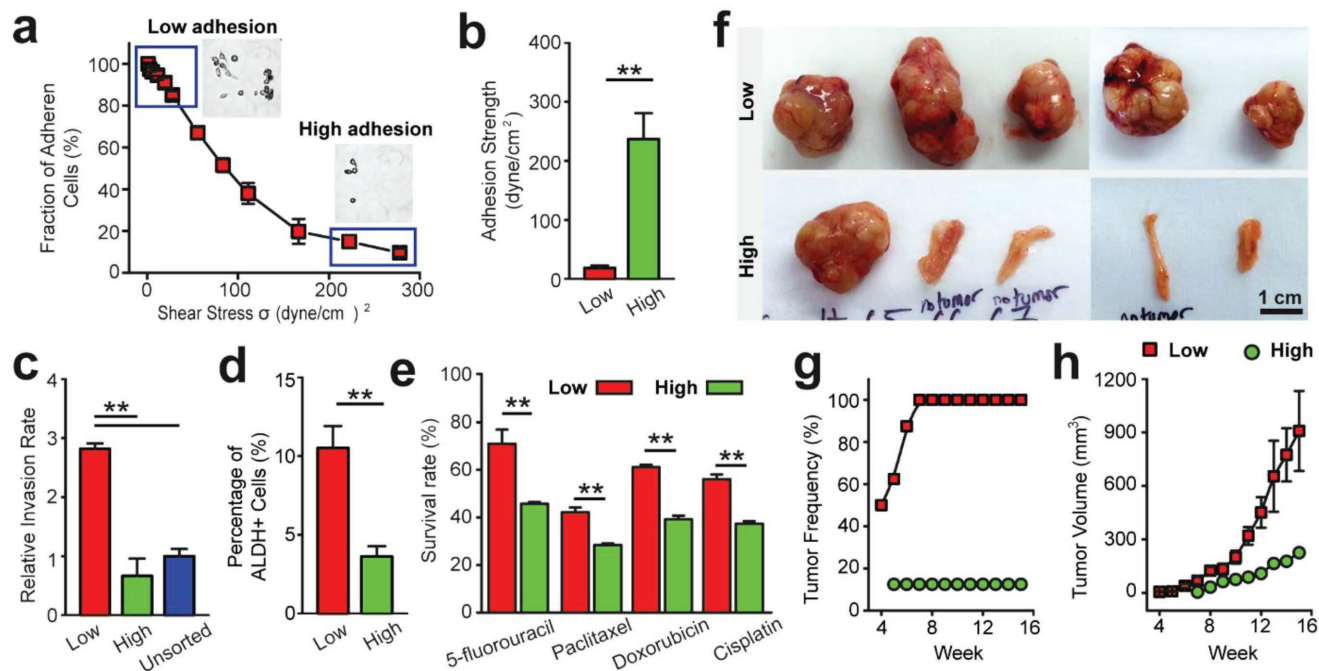
4. Biophysical Selection of CSC-Like IBC Cells and Modulation of IBC Tumorigenic Ability

4.1. Adhesion-Based Selection of CSC-Like IBC Cells

As our study indicated distinct biophysical phenotypes—cell deformability, adhesion, and cellular traction force—for IBC CSCs compared to their non-CSC counterparts, we start to investigate whether we can isolate or modulate those IBC cells with strong tumorigenic ability solely depends on the biophysics distinction between IBC CSCs and non-CSC counterparts. Here, based on the different adhesion strength we observed for IBC CSCs and non-CSCs, we isolated and divided the SUM149 cells into two cell groups with low and high adhesions, and evaluated both their in vitro and in vivo tumorigenic potentials. Briefly, unsorted SUM149 cells were seeded uniformly inside a microfluidic channel for 24 h and then exposure to sustained directional fluids with increasing shear stress on

cells (Figure 3c). Cells of different adhesion strengths detached under different shear stress. The least and most 15% adhesive cells, considered as the "low-adhesion" and "high-adhesion" cells, were separately collected under low and high shear stress flow for further functional analysis (**Figure 5**a,b; see the Experimental Section).

Functional and biophysical analysis of these low-adhesion and high-adhesion cells demonstrated distinct properties. In vitro invasion assays indicated that IBC cells isolated with low adhesion ability (Figure S3a, Supporting Information) had a higher invasive ability compared to high-adhesion and unsorted cells (Figure 5c). ALDEFLUOR analysis by FACS also showed a larger percentage of ALDH+ population in the isolated low-adhesion SUM149 IBC cells compared to high-adhesion cells (Figure 5d). Correspondingly, those isolated low-adhesion SUM149 IBC cells demonstrated higher deformability while the cell diameters of both populations were comparable (Figure S3b–d, Supporting Information). Cell motility examination showed that isolated low-adhesion SUM149 IBC cells demonstrated a significantly higher motility than high-adhesion SUM149 IBC cells (Figure S3e,f, Supporting Information). What is more, when treated low-adhesion and high-adhesion IBC cells with different chemotherapy drugs (5-fluorouracil, paclitaxel, doxorubicin, and cisplatin; Figure 5e—see the

ADVANCED
SCIENCE NEWS
www.advancedsciencenews.com

NANO · MICRO
small
www.small-journal.com

Figure 5. Adhesion-based selection of CSC-like IBC cells with higher tumorigenic ability. a) Fraction of SUM149 cells remaining adherent in the micro-fluidic channel after exposures to sustained directional fluid flow of different shear stress. Inserted brightfield photos show the fraction of SUM149 cells remaining adherent under fluid flow low and high shear stress. b) Quantified adhesion strengths of isolated low-adhesion and high-adhesion SUM149 cells. c) Invasion rate of isolated low-adhesion, high-adhesion, and unsorted SUM149 cells. d) Ratio of ALDH+ cells of isolated low-adhesion and high-adhesion SUM149 IBC cells. e) Survival rate of low-adhesion and high-adhesion SUM 149 cells under treatment of different chemotherapy drugs. f) Photos of tumor growth of low-adhesion and high-adhesion SUM149 cells in xenograft mice. g) Tumor frequency and h) average tumor volumes over time in xenograft mice (total five mice for each group) using isolated low-adhesion and high-adhesion SUM149 cells. For (b), (c), (d), and (e), error bars represent ± s.e.m. *p*-values were calculated using the student *t*-test; ** (*p* < 0.01).

Experimental Section),[72,73] low-adhesion SUM149 IBC cells showed a significant higher survival rate, suggesting a higher intrinsic chemoresistance. Altogether, these in vitro assays demonstrated that low-adhesion SUM149 IBC cells showed a more CSC-like phenotype.

Furthermore, we studied the functional relevance of cell adhesion property with respect to the in vivo tumorigenic ability using a breast cancer xenograft model (Figure 5f–h; see the Experimental Section). To generate tumor xenografts, a small amount of SUM149 IBC cells (1000 cells) of low and high-adhesion cells was injected orthotopically into left inguinal mammary fat pad of each female Ncr nude mouse (5–6 weeks old). The tumorigenicity of low and high-adhesion cells was defined as the frequency of mice with tumors. Tumorigenicity assays revealed that low-adhesion SUM149 cells displayed more efficient tumorigenicity with relatively higher frequency (all five mice formed tumors) than those high-adhesion cells (only one out of five mice formed tumors) (Figure 5f,g). For serial studies of tumorigenesis, tumor volumes were measured weekly till animals were euthanized for tumor burden. Importantly, we found that the tumors generated with low-adhesion cells had a significantly larger average volume than the tumors generated with high-adhesion cells (Figure 5f,h). In addition to the SUM149 IBC cells, we performed the adhesion-based selection of CSC-like cells for another IBC cell line, SUM159. We found that the low-adhesion SUM159 IBC cells showed more CSC-like properties with higher in vitro invasive and in vivo

tumorigenic ability (Figure S4, Supporting Information), which were in consistent with the results from the SUM149 IBC cells. Therefore, we have demonstrated evidence for cancer cell tumorigenic ability determination by cell adhesion property.

4.2. Biophysical Regulation of IBC Cells' Tumorigenic Abilities through the Modulation of IBC Cells' Stiffness

In addition to the adhesion-based selection of CSC-like IBC cells, we explored the potential of controlling CSC population through modulation of the biophysical properties of IBC cells. Many studies showed that substrate rigidity can regulate cell biophysical properties and functions independent of soluble factors.[68] Therefore, utilizing the aforementioned elastic PMA substrates with tunable rigidities, we studied the regulation of IBC cells' tumorigenic abilities through the modulation of IBC cells' stiffness. SUM149 IBC cells were cultured on soft (*E* = 5 kPa) and stiff (*E* = 1200 kPa) PMA substrates for 5 d to allow cells to adapt to the local physical microenvironment and re-modulate their stiffness. To confirm the changes happened in cell stiffness, atomic force microscopy (AFM) was used to measure the stiffness of the adhesive cells at regions far from both the nucleus and lamellipodia (see the Experimental Section and Figure S5 of the Supporting Information).[74] Our AFM measurement result in **Figure 6**a showed a reduced cell stiffness for cells cultured in a soft culture environment.
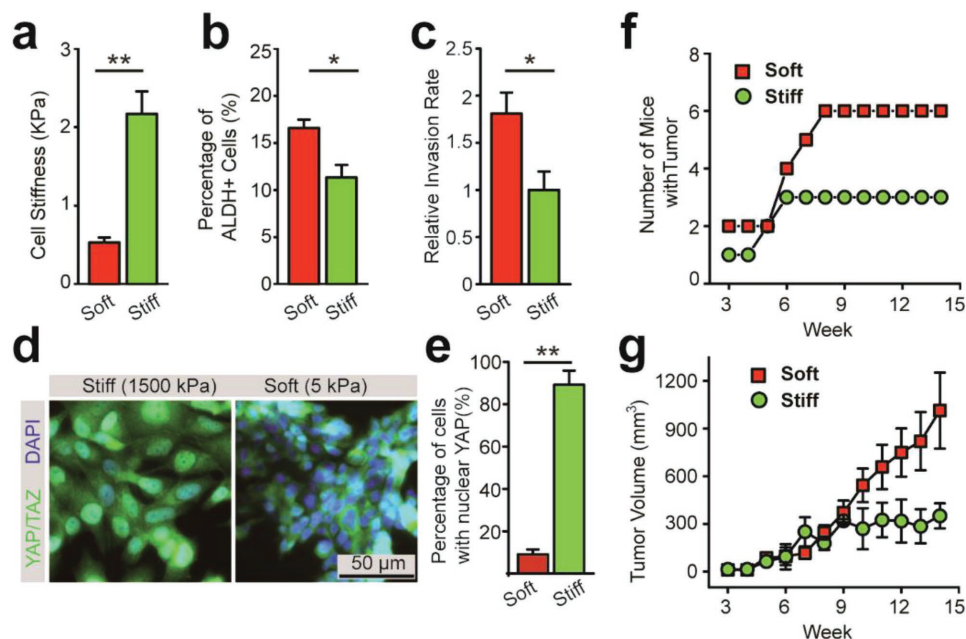
Figure 6. Substrate rigidity regulates IBC cell stiffness and tumorigenicity. a) AFM measured cell stiffness, b) ratio of ALDH+ cells, and c) invasion rate of SUM 149 IBC cells cultured on soft and stiff PMAs. d) Immunostaining images and e) quantified results showing percentages of cells with nuclear YAP/TAZ on stiff and softer PMAs. Nuclear localization of YAP/TAZ was defined if the ratio of nuclear YAP/TAZ over cytoplasmic YAP/TAZ is larger than 1.2. f) Tumor frequency and g) average tumor volumes over time in xenograft mice (total six mice for each group) using SUM 149 cells cultured on soft and stiff PMAs. For (a), (b), (c), and (e), error bars represent ± s.e.m. *p*-values were calculated using the student *t*-test; * ($p < 0.05$) and ** ($p < 0.01$).

Meanwhile, cells cultured in soft culture environment showed a significant higher percentage of ALDH+ cells (Figure 6b). In vitro invasion assays further revealed that soft SUM149 IBC cells cultured on the soft PMAs had a higher invasive ability compared to cells cultured on the stiff substrates (Figure 6c). Further, the Hippo/yes-associated protein (YAP) pathway has been revealed as a critical nuclear-related mechanotransduction pathway that is critically involved in rigidity-dependent cellular sensing and has been shown to involve in stem cell differentiation and tumor-initiation capacities.[75] Our data demonstrated a regulatory effect of ECM rigidity on nucleocytoplasmic shuttling and phosphorylation of YAP/transcriptional coactivator with PDZ-binding motif (TAZ) in SUM149 IBC cells. While YAP/TAZ were predominantly localized in the nucleus for SUM149 IBC cells on stiff substrates ($E = 1200$ kPa), more than 80% of cells on soft ($E = 5$ kPa) showed localization of YAP/TAZ in the cytoplasm (Figure 6d,e). These results indicate that the mechanosensitive YAP/TAZ activity is involved in regulation of IBC cell stiffness and CSC phenotype. Different from researches that indicated a predominate nuclear localization of YAP/TAZ in CSCs,[75] our findings indicate that IBC CSCs defined as ALDH+ SUM149 IBC cells showed a predominate YAP/TAZ cytoplasmic localization. This discrepancy may arise from the fact that breast CSCs exist in both mesenchymal-like and epithelial-like states, and ALDH+ breast CSCs are mostly epithelial-like.[76] Therefore, compared to previous findings using nuclear YAP/TAZ as an indicator of mesenchymal-like CSC phenotype, we discovered that cytoplasmic YAP/TAZ localization feature combined with our identified biophysical features can potentially act as an indicator for IBC CSC phenotype of epithelial-like.

To prove the elevated tumorigenic ability of the soft cells, an in vivo breast cancer xenograft model was used to study the functional relevance of cell stiffness with respect to the tumorigenesis ability (Figure 6f,g; see the Experimental Section). Our in vivo study showed that soft cells formed in the soft environment acquired more efficient tumorigenicity with relatively high frequency (all six mice formed tumors) than those cultured on rigid substrates (only two out of six mice formed tumors) (Figure 6f). More importantly, the tumors generated with soft cells had a significantly larger volume than the tumors generated with stiff cells (Figure 6g). Together, we prove that regulating IBC cell stiffness and the Hippo/YAP pathway can modulate IBC CSC-like phenotype and in turn regulate IBC function and promote or inhibit CSC subpopulation in IBC.

5. Conclusion

CSCs have been proven to initiate tumorigenesis and are the primary population of cells responsible for cancer metastasis in numerous cancer types.[8–14] Within IBC, the ALDH+ population has been shown to represent the tumorigenic and metastatic subpopulation,[8] but detailed studies characterizing the IBC CSC's biophysical properties were lacking. ALDH expression is also negatively correlated with survival outcome[8]; thus, we postulated that the ALDH+ CSCs of IBC would exhibit distinct functional and biophysical properties that would help explain their extremely aggressive metastatic behavior. In our studies, we first examined the migratory and invasive phenotypes of the ALDH+ population in an IBC cell line, SUM149. Utilizing in vitro cell motility and Matrigel invasion assays, we

**ADVANCED
SCIENCE NEWS**
www.advancedsciencenews.com

NANO · MICRO
small
www.small-journal.com

demonstrated a more aggressive phenotype for SUM149 IBC CSCs, which covered a larger migration area and were more successful in invading through a basement membrane mimic. Furthermore, the ALDH+ population could recapitulate the parental cell line heterogeneity and was more slowly cycling than the ALDH− population. These functional characteristics support the fact that the ALDH+ population comprises or is contained within the IBC CSC compartment. Although helpful, these studies only allowed identification of the appropriate group of cells in which to explore metastatic aggressiveness that is potentially derived from cellular biophysical properties. In order to more specifically ascertain and potentially explain the biophysical basis for the aggressive behavior of IBC CSC's, we undertook novel experiments and engineered devices targeted at quantitatively defining cells' biophysical phenotypes. This biophysical characterization of ALDH+ SUM149 IBC CSCs revealed distinct biophysical properties that might mechanistically explain the functional differences seen between the IBC CSC and non-CSC subpopulations. These biophysical properties included a greater cell deformability, weaker adhesion strength, and lower cellular traction force. This unique profile of biophysical characteristics associated with ALDH+ IBC CSCs could help explain how CSCs are better adapted than non-CSCs to successfully navigate through their dynamic microenvironment in the metastatic process.

In the first step of the metastatic cascade, decreased adhesion of IBC CSCs, as demonstrated by their lower measured adhesion strength, might indicate why these cells are able to migrate away from the primary tumor. The strongly adherent ALDH- cells might not be able to overcome their attachment, which is further supported by ALDH− cells' reduced migration capacity in our in vitro studies. Additionally, IBC CSCs, a highly metastatic cell population, showed significantly lower traction forces compared to their non-CSC counterparts, suggesting inherent differences in cell force generation correlated with aggressiveness. In the next steps of the metastatic cascade, migrating cancer cells must invade through the basement membrane and squeeze through endothelial cell tight junctions during intravasation and extravasation. As measured in our assays, the greater capacity for deformation of ALDH+ cells suggests significant plasticity toward cytoskeletal changes or reorganization and underlying mechanical differences in IBC CSCs. This may account in part for their invasive capability to successfully transit through a confining biophysical microenvironment. Cell deformability may thus be used as a label-free biophysical marker for identification and understanding of other CSCs in future studies.

Altogether, we confirmed the functional properties of SUM149 IBC CSCs such as higher migration tendency, invasion, and self-renewal ability, and correlated them with their biophysical properties of increased deformability, decreased adhesion strength, and less contractility. Such a multiparametric profiling can serve as the "biophysical phenotype" of IBC CSCs to biophysically determine cancer cell aggressiveness. This "biophysical phenotype" captures a variety of variations in underlying molecular networks that foster ensemble effects in gross cancer cell properties and behaviors, and therefore may be used as "biophysical marker" for identified IBC CSCs, in addition to molecular markers. More importantly, our studies completed the validation of connections between single cell-level biophysical assessments and the biological tumorigenesis assessed in in vivo murine models. We successfully engineered cellular biophysical properties and deciphered how these cellular biophysical changes are directly associated with cancer tumorigenesis. By selecting IBC cells with low adhesion strength and modulating IBC cells to be soft, IBC cells showed CSC-like characteristics in vitro and enhanced tumorigenicity in in vivo murine models of primary tumor growth, suggesting the determination of IBC CSC phenotype by cell biophysical properties.

Our study provides a more comprehensive understanding of tumorigenesis at the biophysical levels, further suggesting the determination of IBC CSC phenotype by cell biophysical properties. Accurate biophysical phenotyping of CSCs may present potentials for developing mechano-genetically modified cell therapy for targeting and eradicating those CSCs. Regardless of the discovery related to CSCs, the biophysical characterizations and engineering methods in our work can also be applied to map other biological processes that embody cellular biophysical changes, such as EMT and cell aging. The biophysical phenotyping of cancer cells can also be used to preclinically and progressively monitor the effects of various therapeutic agents for cancer treatment. For example, circulating tumor cells can be isolated from patients' blood and subjected to biophysical phenotyping during the treatment process. A successful treatment will significantly reduce the CSC properties in the circulating tumor cells, and thus can be verified by measuring the biophysical properties of these rare cancer cells. Therefore, we believe that our work presents a robust and well-validated study for IBC CSC determination and provides potentials for therapeutic predictions and interventions of cancer treatment.

6. Experimental Section

Cell Culture and Reagents: Two human IBC cell lines SUM149 and SUM159 were obtained from Dr. Stephen P. Ethier at the Medical University of South Carolina. The cell line identity and purity were verified independently. SUM149 and SUM159 cells were cultured in growth medium (Ham's F-12 with L-glutamine, Fisher Scientific, Hanover Park, IL) supplemented with 5% fetal bovine serum (Atlanta Biological, Flowery Branch, GA), 0.5 µg mL^{-1} Fungizone (Thermo Fisher, Carlsbad, CA), 5 µg mL^{-1} Gentamicin (Thermo Fisher, Carlsbad, CA), 5 µg mL^{-1} insulin (MilliporeSigma, St. Louis, MO), 1 µg mL^{-1} hydrocortisone (MilliporeSigma, St. Louis, MO), 50 units mL^{-1} penicillin, and 50 µg mL^{-1} streptomycin. Cells were maintained at 37 °C with 10% CO_2 and 100% humidity. Fresh 0.025% trypsin-ethylenediaminetetraacetic acid (EDTA) in phosphate buffered saline (PBS) was used to re-suspend cells.

ALDEFLUOR Assay: The ALDEFLUOR assay was performed using the ALDEFLOUR Kit (Stemcell Technologies, Vancouver, Canada) according to the manufacturer's instructions.[3] Briefly, ALDEFLUOR treated cells quenched with ALDH inhibitor DEAB were used to set the ALDEFLUOR-positive FACS gate, which was defined as a gate containing less than 0.1% of DEAB-treated cells. Cells treated with ALDEFLUOR alone were then sorted by FACS and used for downstream experiments. Cells above this fluorescence threshold were sorted as ALDH+ and the bottom matching percentage was sorted as ALDH−.

Invasion Assay: In vitro invasion was assayed using the Biocoat Matrigel invasion chamber (BD Biosciences, San Jose, CA). Cells were plated in triplicate in the top portion of the invasion chamber in serum-free medium with 5% serum growth medium in the bottom chamber to induce invasion through the Matrigel membrane. After 24 h of

**ADVANCED
SCIENCE NEWS**

www.advancedsciencenews.com

**NANO · MICRO
small**

www.small-journal.com

incubation, noninvading cells were removed from the top chamber with a cotton swab, and invading cells were fixed with formaldehyde and stained with 1% crystal violet. Matrigel membranes were then removed and de-stained in 10% acetic acid, and a VersaMax optical density reading (Molecular Devices, Sunnyvale, CA) of the acetic acid was taken at 590 nm. In some experiments, Matrigel membranes stained with crystal violet were imaged with invaded cells manually counted.

Cell Motility Assay: The Cellomics Cell Motility kit (Thermo Fisher, Carlsbad, CA) was used to determine cell motility. According to the manufacturer's protocol, single cell suspensions were plated in three wells of a 96-well plate that had previously been coated with blue fluorescent microbeads. After 24 h of incubation, the area a cell migrated was represented by the negative space in the microbead carpet that was pushed away or phagocytosed by the cell. Cells were then fixed, and the migration tracks were imaged using fluorescence microscopy with an Olympus DP26 single chip color CCD camera and an Olympus IX-51 inverted microscope (Olympus, Center Valley, PA). To quantify cell motility, the whole sample surface area was imaged and the image processing software ImageJ (National Institutes of Health, Bethesda, MD) was then used to determine the migration track area of each cell.

Cell Proliferation Assay: Cell proliferation rates were quantified using an MTT Cell Proliferation Assay Kit (Life technologies, Grand Island, NY). Cells were sorted by FACS and plated in triplicate onto 96-well plates. MTT staining and a subsequent optical density reading (Molecular Devices VersaMax) at 590 nm were carried out at 24, 36, 72, and 96 h post sorting.

Scanning electron microscope (SEM) Specimen Preparation: SUM149 cells on PMAs were first washed three times with 50×10^{-3} M Na-cacodylate buffer (pH 7.3; MilliporeSigma, St. Louis, MO). The samples were later fixed for 1 h using 2% glutaraldehyde (Electron Microscopy Sciences, Hatfield, PA) in 50×10^{-3} M Na-cacodylate buffer. After being fixed, the samples were dehydrated in a graded series of ethanol concentrations through 100% over a period of 110 min. Specifically, samples were immersed in 30%, 50%, 70%, 80%, and 90% ethanol for 10 min, separately. At last, the samples were dehydrated in 100% ethanol for three times and each time for 20 min. Afterward, dehydrated substrates were dried with liquid CO_2 using a super critical point dryer (Samdri-PVT-3D, Tousimis, Rockville, MD). Samples were mounted on stubs, sputtered with gold palladium, observed, and photographed under a Hitachi SU8000 Ultra-High Resolution SEM machine (Hitachi High Technologies America, Inc., Pleasanton, CA).

Quantification of Cell Adhesion Rate: Cells were first seeded as single cells in polystyrene 48-well cell culture plates (Thermo Fisher, Carlsbad, CA).[64] The total loading cell number in each sample was first determined using a hemocytometer, and the desired cell concentration was then prepared by serially diluting the original cell suspension with fresh culture medium. After incubation at 10% CO_2 and 37 °C for 3 h, samples were rinsed gently with PBS to remove floating cells. Adherent cells were then labeled with Calcein AM (Thermo Fisher, Carlsbad, CA), before being imaged using fluorescence microscopy (Nikon Eclipse Ti-S, Nikon, Melville, NY). Specifically, to quantify cell adhesion rate, the whole surface area of sample was scanned on a motorized stage (ProScan III, Prior Scientific, Rockland, MA). The images were stitched into a composite and ImageJ was used to determine the number of cells attached to the culture plate surface.

Cell Adhesion Strength Measurements: Cell adhesion strength was quantified as previously described.[64] Briefly, cells in growth medium were first injected into a microfluidic channel by pipette, and the cells were allowed to adhere to the bottom glass surface at 37 °C with 10% CO_2 and 100% humidity for 12 h. An optimized cell loading density (1×10^6 cells mL^{-1}) was used to ensure a uniform seeding of single cells in the microfluidic channel. After cells attached to the bottom glass surface, the microfluidic channel was connected to a syringe pump and a constant flow of PBS was injected into the channel to exert directional fluid shear stress on cells. To remove floating cells before cell adhesion strength measurements, PBS was flowed into the channel with a very low flow rate (10 µL min^{-1} for 1 min and then 30 µL min^{-1} for 1 min). The flow rate was then gradually increased from 100 µL min^{-1} to 2 mL min^{-1} step by step. At each step, the flow rate was maintained constant for 3 min to exert a constant directional fluid shear stress on cells. During the assay, detachment of cells was monitored with a Carl Zeiss Axio Observer Z1 microscope using a 10 × objective (0.3 NA; EC Plan NEOFLUAR; Carl Zeiss MicroImaging, Thornwood, NY). Phase-contrast images were recorded at 15 s intervals for a total period of 3 min. Numbers of adherent cells on the glass surface before and after each step were quantified from the recorded microscope images using ImageJ. The fluidic shear stress (τ_0) exerted on cells was calculated using the equation $\tau_0 = (6\mu Q)/(WH^2)$, where μ is the viscosity of culture medium ($\approx 10^{-3}$ Pa s), Q is the flow rate, and W and H are the microfluidic channel width and height, respectively. The PDMS microfluidic channel used for cell adhesion strength measurements had a channel width W of 2 mm, a channel total length L of 6 mm, and a channel height H of 80 µm. Adhesion strength of cells was defined as the fluidic shear stress at which 50% of cells initially attached on glass surfaces would detach after being exposed to 3 min fluid shear.

Fabrication of PDMS Microfluidic Devices for Cell Deformability and Adhesion Strength Measurements: PDMS microfluidic devices for cell adhesion strength and deformability measurements were fabricated using soft lithography and replica molding.[77] Briefly, a silicon master for microfluidic channels was fabricated using photolithography and deep reactive ion etching (DRIE; STS Deep Silicon Etcher, Surface Technology Systems, Newport, UK). The silicon master was then silanized with (tridecafluoro-1,1,2,2,-tetrahydrooctyl)-1-trichlorosilane vapor (United Chemical Technologies, Bristol, PA) for 4 h under vacuum to facilitate subsequent release of the PDMS microfluidic channel from the silicon master. PDMS prepolymer (Sylgard 184, Dow-Corning, Midland, MI) was then prepared by thoroughly mixing PDMS monomer with curing agent (with the w/w ratio of 10:1), poured onto the silicon master, and cured at 110 °C for 30 min. The fully cured PDMS top layer was then peeled off from the silicon mold, and excess PDMS was trimmed using a razor blade. Through-holes were then punched in the PDMS top layer using a Harris Uni-Core Punch (GE Healthcare Whatman, Piscataway, NJ) to generate microfluidic inlet and outlet holes. The PDMS top layer was then bound to a coverslip substrate using an oxygen plasma-assisted bonding process (Plasma Prep II, West Chester, PA).

Fabrication and Surface Functionalization of PDMS Micropost Array: The PDMS micropost array was fabricated using DRIE and replica molding, as previously described.[68] The silicon micropost array master was first fabricated using photolithography and DRIE. The PDMS micropost array was then generated through a "double casting" process (Figure S2d, Supporting Information). Briefly, the silicon master was first silanized with (tridecafluoro-1,1,2,2,-tetrahydrooctyl)-1-trichlorosilane (Electron Microscopy Sciences, Hatfield, PA) vapor for 4 h under vacuum to facilitate subsequent release of the negative PDMS mold from the silicon master. PDMS prepolymer was then prepared, poured onto the silicon master, and cured at 110 °C for 20 min. The fully cured negative PDMS mold was peeled off from the silicon mold, before being activated with an oxygen plasma for 1 min and silanized with (tridecafluoro-1,1,2,2,-tetrahydrooctyl)-1-trichlorosilane vapor for 24 h. To generate the final PDMS micropost array, 1:10 ratio PDMS prepolymer was poured over the negative PDMS mold and degassed under vacuum for 10 min. A 25 cm × 25 cm cover glass, which served as the substrate for the PDMS micropost array, was then placed on top of the negative PDMS mold. After curing at 110 °C for 40 h, the PDMS micropost array was peeled off from the negative mold to release the final PDMS micropost array. When peeling induced collapse of the PDMS microposts, freestanding PDMS microposts were regenerated by sonication in 100% ethanol for 30 s followed by dry-release with liquid CO_2 using a critical point dryer. The PDMS micropost array used in this study had a post diameter of 1.83 µm, a height of 7.1 µm, and a post center-to-center distance of 4 µm.

Microcontact printing was used to functionalize the PDMS microposts with ECM proteins to promote cell attachment (Figure S2d, Supporting Information). Briefly, a flat 1:30 PDMS stamp was prepared and inked with collagen (BD Biosciences, San Jose, CA) at a saturating concentration of 50 mg mL^{-1} in distilled water for 1 h at room temperature. The PDMS stamp was then thoroughly rinsed with distilled

water and blown dry with nitrogen gas. In parallel, the PDMS micropost array was treated with ultraviolet (UV) ozone (UV-ozone cleaner; Jelight, Irvine, CA) for 7 min to ionize the PDMS surface and thus facilitate transfer of ECM molecules from the stamp to the PDMS micropost tops. The collagen-coated PDMS stamp was then gently placed in conformal contact with the PDMS micropost array for 30 s to complete the protein transfer process. To utilize the PDMS micropost array for live-cell traction force measurements, we stained the PDMS micropost with 1,1′-dioleyl-3,3,3′,3′-tetramethylindocarbocyanine methanesulfonate (Δ^9-DiI; Thermo Fisher, Carlsbad, CA). Pluronic F127 NF (0.2%, w/v; BASF, Ludwigshafen, Germany) dissolved in PBS (MilliporeSigma, St. Louis, MO) was then adsorbed to the PDMS surface for 1 h at room temperature to prevent protein adsorption to nonfunctionalized portions of the PDMS micropost array.

Cell Deformability Measurements: The cell deformability was measured using a PDMS-based microfluidic deformability microcytometer developed in our lab as previously described.[33] The deformability microcytometer contains an array of funnel-shaped long confining microchannels that trap individual live cancer cells in each channel for single cell deformability measurement. Each channel has a length of 300 µm, a height of 30 µm, a width at the wide end (entry) of 30 µm, and a width at the narrow end of 4 µm. The channel wall is precoated with Pluronic-127 (MilliporeSigma, St. Louis, MO) for 30 min such that friction between the cell and the channel wall can be neglected. Single cancer cells in suspension are first loaded into the channel using a pressure pump (ELVESYS, Paris, French) under low pressure (0.1–0.5 kPa). The differential pressure acting on cancer cells will gradually push the cells down the funnel, and ultimately the motion of cancer cells will stop due to the confining channel and the cells will be trapped in place. After the cell trapping, the loading pressure is gradually increased in steps (0.5 kPa for each step) to push the cell further into the channel. The trapped cells will have different deformation under different pressure. For inert microfluidic channels where cell trapping is dictated by steric interactions of cancer cells with the confining channel, the penetration length (L) of individual cancer cells into the confining channel will be purely determined by cell size and deformability. Thereby, the single cell deformability can be calculated based on model equation Deformability = $16.9 \times d \times (A \times \Delta P)^{-1}$, where ΔP is the change of the flow pressure, d is the penetrating length under the pressure change, and A is the projective area of the cell. Cell volume V is calculated as $V = (4 \times A \times \pi^{-1})^{-1/2}$. During the assay, deformed cells were monitored with the Carl Zeiss Axio Observer Z1 microscope using a 10× objective (0.3 NA; EC Plan NEOFLUAR; Carl Zeiss MicroImaging). Phase-contrast images were recorded. The penetration length (L) and the longitudinal and lateral diameters (D_{long} and D_{lat}) of each cell for each pressure were quantified from the recorded microscope images using ImageJ (National Institutes of Health, Bethesda, MD) to calculate the projective area of the cell $A \approx 0.25\pi \times D_{long} \times D_{lat}$.

Cell Stiffness Measurement Using AFM: An AFM Bruker Dimension Icon instrument (Bruker, Billerica, MA) was used for cell stiffness measurement.[74] Before indentation on cells, the deflection sensitivity of the cantilever deflection was calibrated to convert photodiode signal from voltage to nanometer by obtaining force curves on a clean glass slide and measuring their slope values. Spring constant of the cantilever was obtained under thermal tune option. The clean glass slide was then replaced by PMA samples with cells cultured on it. Indentation experiments were performed in the cell culture medium at room temperature using the contact point-based mode in fluid. The cells on PMA were indented by a spherical probe (2500 nm in radius) attached to one end of an AFM cantilever. Cell stiffness was measured by indenting each cell at four distinct spots under the script mode. The four measurements were averaged for each cell and defined as the cell stiffness.

Quantification of Cell Traction Force: Cell traction forces were quantified as previously described.[68,69] In brief, phase-contrast images of live cells and fluorescence images of Δ^9-DiI stained PDMS microposts underlying the cells were taken at the focal plane passing through the top surface of the posts with a 40 × objective on the Zeiss Observer Z1 microscope attached with the AxioCam camera. The microscope was enclosed in the Carl Zeiss XL S1 environmental chamber to maintain

the experimental environment at 37 °C and 10% CO_2. Images were then analyzed with a custom-developed MATLAB program to calculate the deflection δ of the post centroid from its ideal position determined by the free and undeflected posts, which was then converted to the horizontal traction force f using the expression $f = K\delta$, where K was the nominal spring constant of the PDMS micropost calculated from the Euler–Bernoulli beam theory as $K = 3\pi ED^4/(64H^3)$. In this equation, E is the elastic Young's modulus of PDMS and D and H are post diameter and height, respectively.

Microfluidic Isolation of Low-Adhesion and High-Adhesion Cells: The microfluidic channel device used for low-adhesion and high-adhesion cell isolation was the same as that used to measure cell adhesion strength. Briefly, unsorted SUM149 or SUM159 cells in growth medium were first injected into the microfluidic channel by pipette, and the cells were incubated in the microfluidic channel at 37 °C with 10% CO_2 and 100% humidity for 12 h. After 12 h of incubation, the microfluidic channel was connected to a syringe pump. To remove floating cells before cell isolation, PBS was flowed into the channel with a very low flow rate (10 µL min^{-1} for 1 min and then 30 µL min^{-1} for 1 min). After washed away floating cells, TrypLE (1X, Thermal Fisher) diluted 50 times in PBS was flowed into the channel and gradually increased from 40 µL min^{-1} to 10 mL min^{-1} step by step. Low-adhesion cells were collected when using low flow rate (low shear stress) from 40 µL min^{-1} to 1 mL min^{-1}; and high-adhesion cells were collected when using high flow rate (high shear stress) from 8 mL min^{-1} to 10 mL min^{-1}. During the isolation, detachment of cells was monitored with a Carl Zeiss Axio Observer Z1 microscope using a 10 × objective (0.3 NA; EC Plan NEOFLUAR; Carl Zeiss MicroImaging, Thornwood, NY).

Chemotherapy Drug Treatment: To test the drug resistance of isolated IBC cells, low-adhesion and high-adhesion SUM149 IBC cells were seeded at the same density in 6-well plate and were incubated at 37 °C with 10% CO_2 and 100% humidity. Chemotherapy drugs, 5×10^{-3} M 5-fluorouracil (MilliporeSigma, St. Louis, MO), 10×10^{-9} M paclitaxel (MilliporeSigma, St. Louis, MO), 100×10^{-9} M doxorubicin (MilliporeSigma, St. Louis, MO), and 10×10^{-6} M cisplatin (MilliporeSigma, St. Louis, MO) were added to the SUM 149 cell culture media for 24 h, respectively.[73] Under each condition, the number of survival cells was counted and compared to control without any drug treatment. Survival rate was calculated as the ratio of the number of survival cells to the initial loaded cells.

Tumorigenicity Mouse Models: Care of animals and experimental procedures were according to the University of Michigan University Committee on Use and Care of Animals (UCUCA) approved protocols #PRO5314 and #PRO4116. To generate breast cancer xenografts and evaluate cell tumorigenic potentials, a small amount of SUM149 or SUM159 IBC cells (1000 cells) collected from low-adhesion and high-adhesion cells and cells collected from soft and stiff PMAs were injected orthotopically into the left inguinal mammary fat pad of each female Ncr nude mouse (Taconic Biosciences, Rensselaer, NY), respectively. The cells were suspended in 50 µL PBS and 50 µL Matrigel (Becton Dickinson). Tumor growth was monitored weekly by caliper measurement with ellipsoid volumes calculated using ½ × length × width × height.

Statistics: p-value was calculated using the student t-test function in Excel (Microsoft, Seattle, WA). At least four independent experiments were performed for each ALDEFLUOR analysis, immunostaining, in vitro invasion, migration, and MTT Cell Proliferation, chemoresistance assay, as well as in vitro cell deformability, cell adhesion strength, cell traction force measurement, and the in vivo tumorigenesis study in xenograft mice.

Supporting Information

Supporting Information is available from the Wiley Online Library or from the author.

Acknowledgements

Conflict of Interest

The authors declare no conflict of interest.

Keywords

biophysical property, cancer stem cells, inflammatory breast cancer

[1] F. M. Robertson, M. Bondy, W. Yang, H. Yamauchi, S. Wiggins, S. Kamrudin, S. Krishnamurthy, H. Le-Petross, L. Bidaut, A. N. Player, S. H. Barsky, W. A. Woodward, T. Buchholz, A. Lucci, N. T. Ueno, M. Cristofanilli, *Ca-Cancer J. Clin.* **2010**, *60*, 351.

[2] H. Yamauchi, W. A. Woodward, V. Valero, R. H. Alvarez, A. Lucci, T. A. Buchholz, T. Iwamoto, S. Krishnamurthy, W. Yang, J. M. Reuben, G. N. Hortobagyi, N. T. Ueno, *Oncologist* **2012**, *17*, 891.

[3] D. T. Rosenthal, J. Zhang, L. Bao, L. Zhu, Z. Wu, K. Toy, C. G. Kleer, S. D. Merajver, *PLoS One* **2012**, *7*, e40979.

[4] F. M. Robertson, E. F. Petricoin Iii, S. J. Van Laere, F. Bertucci, K. Chu, S. V. Fernandez, Z. Mu, K. Alpaugh, J. Pei, R. Circo, J. Wulfkuhle, Z. Ye, K. M. Boley, H. Liu, R. Moraes, X. Zhang, R. Demaria, S. H. Barsky, G. Sun, M. Cristofanilli, *SpringerPlus* **2013**, *2*, 497.

[5] T. Reya, S. J. Morrison, M. F. Clarke, I. L. Weissman, *Nature* **2001**, *414*, 105.

[6] M. R. Alison, S. Islam, N. A. Wright, *J. Cell Sci.* **2010**, *123*, 2357.

[7] C. T. Jordan, M. L. Guzman, M. Noble, *N. Engl. J. Med.* **2006**, *355*, 1253.

[8] E. Charafe-Jauffret, C. Ginestier, F. Iovino, C. Tarpin, M. Diebel, B. Esterni, G. Houvenaeghel, J. M. Extra, F. Bertucci, J. Jacquemier, L. Xerri, G. Dontu, G. Stassi, Y. Xiao, S. H. Barsky, D. Birnbaum, P. Viens, M. S. Wicha, *Clin. Cancer Res.* **2010**, *16*, 45.

[9] M. Al-Hajj, M. S. Wicha, A. Benito-Hernandez, S. J. Morrison, M. F. Clarke, *Proc. Natl. Acad. Sci. USA* **2003**, *100*, 3983.

[10] S. K. Singh, I. D. Clarke, M. Terasaki, V. E. Bonn, C. Hawkins, J. Squire, P. B. Dirks, *Cancer Res.* **2003**, *63*, 5821.

[11] A. T. Collins, P. A. Berry, C. Hyde, M. J. Stower, N. J. Maitland, *Cancer Res.* **2005**, *65*, 10946.

[12] H. Liu, M. R. Patel, J. A. Prescher, A. Patsialou, D. Qian, J. Lin, S. Wen, Y. F. Chang, M. H. Bachmann, Y. Shimono, P. Dalerba, M. Adorno, N. Lobo, J. Bueno, F. M. Dirbas, S. Goswami, G. Somlo, J. Condeelis, C. H. Contag, S. S. Gambhir, M. F. Clarke, *Proc. Natl. Acad. Sci. USA* **2010**, *107*, 18115.

[13] P. C. Hermann, S. L. Huber, T. Herrler, A. Aicher, J. W. Ellwart, M. Guba, C. J. Bruns, C. Heeschen, *Cell Stem Cell* **2007**, *1*, 313.

[14] R. Pang, W. L. Law, A. C. Chu, J. T. Poon, C. S. Lam, A. K. Chow, L. Ng, L. W. Cheung, X. R. Lan, H. Y. Lan, V. P. Tan, T. C. Yau, R. T. Poon, B. C. Wong, *Cell Stem Cell* **2010**, *6*, 603.

[15] L. Ricci-Vitiani, D. G. Lombardi, E. Pilozzi, M. Biffoni, M. Todaro, C. Peschle, R. De Maria, *Nature* **2007**, *445*, 111.

[16] C. Ginestier, M. H. Hur, E. Charafe-Jauffret, F. Monville, J. Dutcher, M. Brown, J. Jacquemier, P. Viens, C. G. Kleer, S. L. Liu, A. Schott, D. Hayes, D. Birnbaum, M. S. Wicha, G. Dontu, *Cell Stem Cell* **2007**, *1*, 555.

[17] P. Dalerba, S. J. Dylla, I. K. Park, R. Liu, X. Wang, R. W. Cho, T. Hoey, A. Gurney, E. H. Huang, D. M. Simeone, A. A. Shelton, G. Parmiani, C. Castelli, M. F. Clarke, *Proc. Natl. Acad. Sci. USA* **2007**, *104*, 10158.

[18] S. J. Dylla, L. Beviglia, I. K. Park, C. Chartier, J. Raval, L. Ngan, K. Pickell, J. Aguilar, S. Lazetic, S. Smith-Berdan, M. F. Clarke, T. Hoey, J. Lewicki, A. L. Gurney, *PLoS One* **2008**, *3*, e2428.

[19] T. Teramura, K. Fukuda, S. Kurashimo, Y. Hosoi, Y. Miki, S. Asada, C. Hamanishi, *BMC Musculoskeletal Disord.* **2008**, *9*, 86.

[20] K. R. Leventhal, H. Yu, L. Kass, J. N. Lakins, M. Egeblad, J. T. Erler, S. F. Fong, K. Csiszar, A. Giaccia, W. Weninger, M. Yamauchi, D. L. Gasser, V. M. Weaver, *Cell* **2009**, *139*, 891.

[21] R. Jinka, R. Kapoor, P. G. Sistla, T. A. Raj, G. Pande, *Int. J. Cell Biol.* **2012**, *2012*, 1.

[22] T. R. Cox, J. T. Erler, *Dis. Models Mech.* **2011**, *4*, 165.

[23] F. Berthiaume, P. V. Moghe, M. Toner, M. L. Yarmush, *FASEB J.* **1996**, *10*, 1471.

[24] M. J. Paszek, N. Zahir, K. R. Johnson, J. N. Lakins, G. I. Rozenberg, A. Gefen, C. A. Reinhart-King, S. S. Margulies, M. Dembo, D. Boettiger, D. A. Hammer, V. M. Weaver, *Cancer Cell* **2005**, *8*, 241.

[25] J. I. Lopez, I. Kang, W. K. You, D. M. McDonald, V. M. Weaver, *Integr. Biol.* **2011**, *3*, 910.

[26] S. Kumar, V. M. Weaver, *Cancer Metastasis Rev.* **2009**, *28*, 113.

[27] P. F. Davies, J. A. Spaan, R. Krams, *Ann. Biomed. Eng.* **2005**, *33*, 1714.

[28] D. E. Ingber, *Ann. Med.* **2003**, *35*, 564.

[29] V. Swaminathan, K. Mythreye, E. T. O'Brien, A. Berchuck, G. C. Blobe, R. Superfine, *Cancer Res.* **2011**, *71*, 5075.

[30] S. Suresh, *Acta Biomater.* **2007**, *3*, 413.

[31] P. Katira, R. T. Bonnecaze, M. H. Zaman, *Front. Oncol.* **2013**, *3*, 145.

[32] M. Lekka, K. Pogoda, J. Gostek, O. Klymenko, S. Prauzner-Bechcicki, J. Wiltowska-Zuber, J. Jaczewska, J. Lekki, Z. Stachura, *Micron* **2012**, *43*, 1259.

[33] S. H. Hu, G. Y. Liu, W. Q. Chen, X. Li, W. Lu, R. H. W. Lam, J. P. Fu, *Small* **2016**, *12*, 2300.

[34] W. W. Xu, R. Mezencev, B. Kim, L. J. Wang, J. McDonald, T. Sulchek, *PLoS One* **2012**, *7*, e46609.

[35] S. Byun, S. Son, D. Amodei, N. Cermak, J. Shaw, J. H. Kang, V. C. Hecht, M. M. Winslow, T. Jacks, P. Mallick, S. R. Manalis, *Proc. Natl. Acad. Sci. USA* **2013**, *110*, 7580.

[36] D. Wirtz, K. Konstantopoulos, P. C. Searson, *Nat. Rev. Cancer* **2011**, *11*, 512.

[37] R. J. Pelham Jr., Y. Wang, *Proc. Natl. Acad. Sci. USA* **1997**, *94*, 13661.

[38] D. A. Lauffenburger, A. F. Horwitz, *Cell* **1996**, *84*, 359.

[39] W. Chen, Y. Sun, J. Fu, *Small* **2013**, *9*, 81.

[40] S. Weng, J. Fu, *Biomaterials* **2011**, *32*, 9584.

[41] Z. Li, J. Song, G. Mantini, M.-Y. Lu, H. Fang, C. Falconi, L.-J. Chen, Z. L. Wang, *Nano Lett.* **2009**, *9*, 3575.

[42] H. Feng, H. Ouyang, M. Peng, Y. Jin, Y. Zhang, Z. Liu, Y. Zou, C. Zhao, Y. Fan, J. Zhai, Z. L. Wang, Z. Li, *Nano Energy* **2018**, *50*, 504.

[43] C. T. Mierke, P. Bretz, P. Altevogt, *J. Biol. Chem.* **2011**, *286*, 34858.

[44] C. M. Kraning-Rush, J. P. Califano, C. A. Reinhart-King, *PLoS One* **2012**, *7*, e32572.

[45] M. Magni, S. Shammah, R. Schiro, W. Mellado, R. Dalla-Favera, A. M. Gianni, *Blood* **1996**, *87*, 1097.

[46] Y. Luo, K. Dallaglio, Y. Chen, W. A. Robinson, S. E. Robinson, M. D. McCarter, J. Wang, R. Gonzalez, D. C. Thompson, D. A. Norris, D. R. Roop, V. Vasiliou, M. Fujita, *Stem Cells* **2012**, *30*, 2100.

[47] V. Vasiliou, A. Pappa, T. Estey, *Drug Metab. Rev.* **2004**, *36*, 279.

[48] A. K. Croker, D. Goodale, J. Chu, C. Postenka, B. D. Hedley, D. A. Hess, A. L. Allan, *J. Cell. Mol. Med.* **2009**, *13*, 2236.

[49] E. Charafe-Jauffret, C. Ginestier, D. Birnbaum, *BMC Cancer* **2009**, *9*, 202.

[50] P. Marcato, C. A. Dean, D. Pan, R. Araslanova, M. Gillis, M. Joshi, L. Helyer, L. Pan, A. Leidal, S. Gujar, C. A. Giacomantonio, P. W. K. Lee, *Stem Cells* **2011**, *29*, 32.

[51] T. Tanei, K. Morimoto, K. Shimazu, S. J. Kim, Y. Tanji, T. Taguchi, Y. Tamaki, S. Noguchi, *Clin. Cancer Res.* **2009**, *15*, 4234.

[52] F. Jiang, Q. Qiu, A. Khanna, N. W. Todd, J. Deepak, L. X. Xing, H. J. Wang, Z. Q. Liu, Y. Su, S. A. Stass, R. L. Katz, *Mol. Cancer Res.* **2009**, *7*, 330.

[53] D. Ucar, C. R. Cogle, J. R. Zucali, B. Ostmark, E. W. Scott, R. Zori, B. A. Gray, J. S. Moreb, *Chem.-Biol. Interact.* **2009**, *178*, 48.

[54] S. Ma, K. W. Chan, T. K. W. Lee, K. H. Tang, J. Y. H. Wo, B. J. Zheng, X. Y. Guan, *Mol. Cancer Res.* **2008**, *6*, 1146.

[55] J. E. Carpentino, M. J. Hynes, H. D. Appelman, T. Zheng, D. A. Steindler, E. W. Scott, E. H. Huang, *Cancer Res.* **2009**, *69*, 8208.

[56] Z. A. Rasheed, J. Yang, Q. Wang, J. Kowalski, I. Freed, C. Murter, S. M. Hong, J. B. Koorstra, N. V. Rajeshkumar, X. He, M. Goggins, C. Iacobuzio-Donahue, D. M. Berman, D. Laheru, A. Jimeno, M. Hidalgo, A. Maitra, W. Matsui, *JNCI, J. Natl. Cancer Inst.* **2010**, *102*, 340.

[57] I. A. Silva, S. M. Bai, K. McLean, K. Yang, K. Griffith, D. Thomas, C. Ginestier, C. Johnston, A. Kueck, R. K. Reynolds, M. S. Wicha, R. J. Buckanovich, *Cancer Res.* **2011**, *71*, 3991.

[58] Y. C. Chen, Y. W. Chen, H. S. Hsu, L. M. Tseng, P. I. Huang, K. H. Lu, D. T. Chen, L. K. Tai, M. C. Yung, S. C. Chang, H. H. Ku, S. H. Chiou, W. L. Lo, *Biochem. Biophys. Res. Commun.* **2009**, *385*, 307.

[59] C. van den Hoogen, G. van der Horst, H. Cheung, J. T. Buijs, J. M. Lippitt, N. Guzman-Ramirez, F. C. Hamdy, C. L. Eaton, G. N. Thalmann, M. G. Cecchini, R. C. Pelger, G. van der Pluijm, *Cancer Res.* **2010**, *70*, 5163.

[60] P. B. Gupta, C. M. Fillmore, G. Jiang, S. D. Shapira, K. Tao, C. Kuperwasser, E. S. Lander, *Cell* **2011**, *146*, 633.

[61] C. L. Chaffer, I. Brueckmann, C. Scheel, A. J. Kaestli, P. A. Wiggins, L. O. Rodrigues, M. Brooks, F. Reinhardt, Y. Su, K. Polyak, L. M. Arendt, C. Kuperwasser, B. Bierie, R. A. Weinberg, *Proc. Natl. Acad. Sci. USA* **2011**, *108*, 7950.

[62] P. Van Wachem, T. Beugeling, J. Feijen, A. Bantjes, J. Detmers, W. Van Aken, *Biomaterials* **1985**, *6*, 403.

[63] F. Grinnell, M. Milam, P. A. Srere, *Biochem. Med.* **1973**, *7*, 87.

[64] W. Q. Chen, S. N. Weng, F. Zhang, S. Allen, X. Li, L. W. Bao, R. H. W. Lam, J. A. Macoska, S. D. Merajver, J. P. Fu, *ACS Nano* **2013**, *7*, 566.

[65] K. V. Christ, K. T. Turner, *J. Adhes. Sci. Technol.* **2010**, *24*, 2027.

[66] K. W. Kwon, S. S. Choi, S. H. Lee, B. Kim, S. N. Lee, M. C. Park, P. Kim, S. Y. Hwang, K. Y. Suh, *Lab Chip* **2007**, *7*, 1461.

[67] E. W. Young, A. R. Wheeler, C. A. Simmons, *Lab Chip* **2007**, *7*, 1759.

[68] J. Fu, Y. K. Wang, M. T. Yang, R. A. Desai, X. Yu, Z. Liu, C. S. Chen, *Nat. Methods* **2010**, *7*, 733.

[69] M. T. Yang, J. Fu, Y. K. Wang, R. A. Desai, C. S. Chen, *Nat. Protoc.* **2011**, *6*, 187.

[70] Z. Fan, Y. Sun, C. Di, D. Tay, W. Chen, C. X. Deng, J. Fu, *Sci. Rep.* **2013**, *3*, 2176.

[71] G. W. Brodland, J. H. Veldhuis, *PLoS One* **2012**, *7*, e44281.

[72] J. Liu, Y. Tan, H. Zhang, Y. Zhang, P. Xu, J. Chen, Y.-C. Poh, K. Tang, N. Wang, B. Huang, *Nat. Mater.* **2012**, *11*, 734.

[73] C. M. Fillmore, C. Kuperwasser, *Breast Cancer Res.* **2008**, *10*, R25.

[74] N. Nguyen, Y. Shao, A. Wineman, J. Fu, A. Waas, *Math. Biosci.* **2016**, *277*, 77.

[75] F. Zanconato, M. Cordenonsi, S. Piccolo, *Cancer Cell* **2016**, *29*, 783.

[76] S. Liu, Y. Cong, D. Wang, Y. Sun, L. Deng, Y. Liu, R. Martin-Trevino, L. Shang, S. P. McDermott, M. D. Landis, *Stem Cell Rep.* **2014**, *2*, 78.

[77] W. Chen, S. G. Allen, A. K. Reka, W. Qian, S. Han, J. Zhao, L. Bao, V. G. Keshamouni, S. D. Merajver, J. Fu, *BMC Cancer* **2016**, *16*, 614.